nature COMMUNICATIONS

ARTICLE

Received 6 Jul 2014 | Accepted 11 Dec 2014 | Published 14 Jan 2015

DOI: 10.1038/ncomms7088

Probing the electron states and metal-insulator transition mechanisms in molybdenum disulphide vertical heterostructures

Xiaolong Chen[1], Zefei Wu[1], Shuigang Xu[1], Lin Wang[2], Rui Huang[1,3], Yu Han[1], Weiguang Ye[1], Wei Xiong[1], Tianyi Han[1], Gen Long[1], Yang Wang[1], Yuheng He[1], Yuan Cai[1], Ping Sheng[1] & Ning Wang[1]

The metal-insulator transition is one of the remarkable electrical properties of atomically thin molybdenum disulphide. Although the theory of electron–electron interactions has been used in modelling the metal-insulator transition in molybdenum disulphide, the underlying mechanism and detailed transition process still remain largely unexplored. Here we demonstrate that the vertical metal-insulator-semiconductor heterostructures built from atomically thin molybdenum disulphide are ideal capacitor structures for probing the electron states. The vertical configuration offers the added advantage of eliminating the influence of large impedance at the band tails and allows the observation of fully excited electron states near the surface of molybdenum disulphide over a wide excitation frequency and temperature range. By combining capacitance and transport measurements, we have observed a percolation-type metal-insulator transition, driven by density inhomogeneities of electron states, in monolayer and multilayer molybdenum disulphide. In addition, the valence band of thin molybdenum disulphide layers and their intrinsic properties are accessed.

[1] Department of Physics and the William Mong Institute of Nano Science and Technology, Hong Kong University of Science and Technology, Clear Water Bay, Kowloon, Hong Kong, China. [2] Department of Condensed Matter Physics, Group of Applied Physics, University of Geneva, 24 Quai Ernest Ansermet, CH1211 Geneva, Switzerland. [3] Department of Physics and Electronic Engineering, Hanshan Normal University, Chaozhou, Guangdong 521041, China. Correspondence and requests for materials should be addressed to N.W. (email: phwang@ust.hk).

© 2015 Macmillan Publishers Limited. All rights reserved.

Molybdenum disulphide (MoS_2), an *n*-type semiconductor[1–16], shows novel properties such as superconductivity[6], controllable valley polarization[17,18] and metal-insulator transition[3–6] (MIT). In MoS_2 field-effect transistors (FETs), gate-induced charge carriers transport in a thin layer near the surface of MoS_2 and are vulnerable to charge impurities and different types of disorder[2,3,12,14,19,20]. The presence of a high-κ dielectric material[3] to monolayer MoS_2 can effectively screen charge impurities and allow the observation of MIT. Based on recent transport measurements[3], the phase transition behaviour of monolayer MoS_2 has been attributed to transition from an insulating phase, in which disorder suppresses the electronic interactions, to a metallic phase in which strong coulomb interactions occur. However, the underlying physical mechanism and detailed MIT process need to be further clarified. Different from the studies on transport properties of MoS_2, the capacitance spectroscopy[14] recently applied to the characterization of MoS_2 FET structures has been demonstrated as one of the most convenient and powerful method for studying the electron states in MoS_2 at room temperature. At low temperatures, however, the information obtained by this technique is limited due to the large impedance near the band edge of MoS_2. Different from that in graphene quantum capacitors[21–27], the slow charge-carrier mobility in MoS_2 capacitors often leads to incompletely charged states, mainly due to the localization near the band edge. The incompletely charged capacitance confuses the effect of charge traps.

In the following, we show an approach to address these problems by introducing a MoS_2-based vertical metal-insulator-semiconductor-metal (MIS-M) heterostructure suitable for probing electron states using capacitance measurements. Unlike conventional FET structures[14], our approach eliminates the impedance effects and can directly access the intrinsic characteristics of thin-layer MoS_2 over a wide frequency (100 Hz–1 MHz) and temperature range (2–300 K). By combining capacitance and transport measurements, we show that the MIT observed in monolayer and multilayer MoS_2 is consistent with the physical picture of a percolation[28–35] transition model. The results of our investigation on the mechanisms of MIT and other intrinsic characteristics, such as thickness-dependent screening abilities and fast relaxation of hole carriers at the valence band, provide useful information much needed for improving the performance of the FET devices based on MoS_2 monolayers and multilayers.

Results

MoS_2 vertical heterostructural capacitance devices. Figure 1a,b illustrates our specially designed MIS-M capacitor device, fabricated by transferring[23,36] exfoliated flakes of MoS_2 and hexagonal boron nitride (BN) on a Si substrate coated with a SiO_2 thin layer (300 nm). Exfoliated natural crystals of monolayer or multilayer MoS_2 were first transferred onto a BN sheet, serving as an ultra-smooth and disorder-free gate dielectric[37]. A Ti/Au (10 nm/20 nm) local gate sits underneath the BN sheet. The critical step in achieving MIS-M structure is to have the MoS_2 sheet fully covered by a top electrode (Ti/Au: 10 nm/50 nm). The equivalent circuit of this device geometry is shown in Fig. 1c. The measured capacitance C_t is the total capacitance contributed by two capacitors originating from MoS_2 (C_{MoS}) and the geometric capacitor (C_g) in serial connection, plus the residual capacitance C_p in parallel connection. C_t, shown below, is the capacitance wiping off C_p (see detailed analysis in Supplementary Figs 1–3 and Supplementary Note 1 and 2). Therefore, $C_t = (C_{MoS}^{-1} + C_g^{-1})^{-1}$. With fully covered top electrodes, carriers can respond vertically instead of moving in

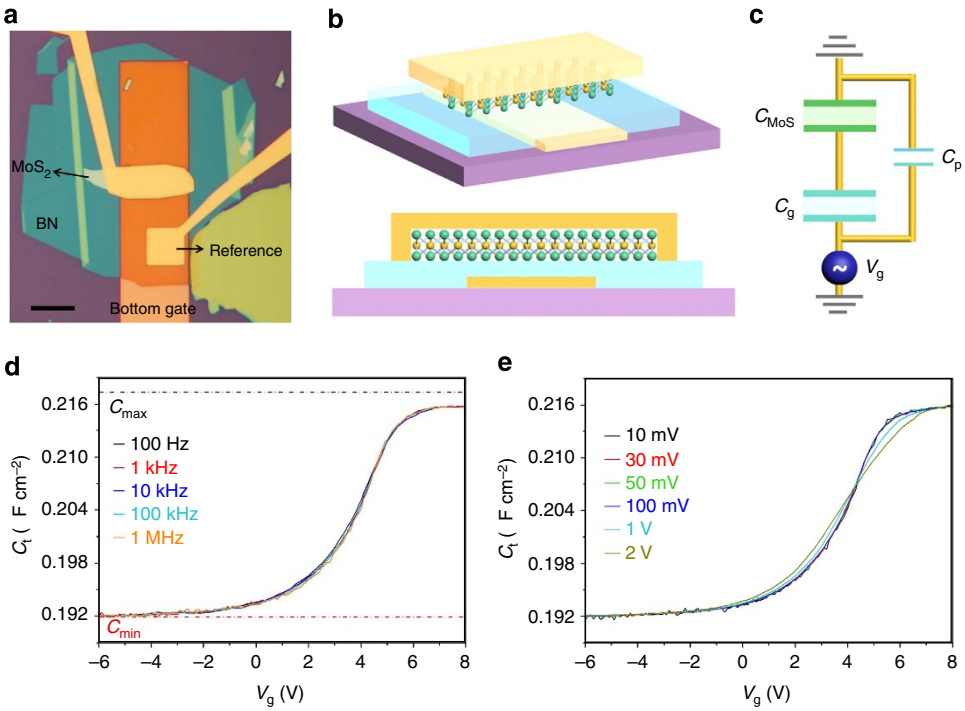

Figure 1 | The optical and schematic images of the MoS_2 MIS-M heterostructures. (**a**,**b**) The MoS_2 flakes are fully covered by a top Ti/Au electrode. The square top electrode in **a** is the reference capacitor. Scale bar, 10 μm. (**c**) The equivalent circuit of the MoS_2 capacitance devices. Total capacitance C_t measured from a 5.9-nm-thick MoS_2 at 2 K at different frequencies (**d**) and excitation voltages (**e**), respectively. The measured capacitance in vertical heterostructures is almost independent of excitation frequencies, which differs greatly from that obtained in conventional FET structures (Supplementary Fig. 4). The excitation voltage used for **d** is 50 mV and the frequency used for **e** is 100 kHz.

© 2015 Macmillan Publishers Limited. All rights reserved.

the plane of MoS_2. This unique structure directly avoids the huge lateral resistance R of MoS_2 near the band edge. As a result, the measured C_t (of a 5.9-nm-thick MoS_2) at 2 K (Fig. 1d) is almost independent of excitation frequencies f, which differs greatly from that obtained in conventional FET structure devices[7,14]. In capacitance measurement of conventional FET structures, lateral resistance R must be considered when $R \sim 1/(2\pi f C_t)$. This is confirmed by our MoS_2 capacitance devices with partially covered top electrodes, which show significant frequency-dependent and temperature-dependent characteristics (Supplementary Fig. 4 and Supplementary Note 3). We also achieved good Ohmic contacts between the top Ti/Au electrode and MoS_2 in our devices, as evidenced by the capacitance measurements at different excitation voltages (Fig. 1e). Note that the capacitance measured at large excitation voltages (for example, at 2 V) shows deviation due to the averaging effect.

Characterization of the vertical MIS-M structures. The interface structure and band diagrams in the MoS_2-based MIS-M devices are shown schematically in Fig. 4a–d. When the gate voltage $V_g > 0$, electrons accumulate at the MoS_2 surface (Fig. 4b). The measured capacitance approaches the geometric capacitance $C_{max} = C_g$ when V_g is sufficiently large, while under negative V_g (Fig. 4c) electrons are depleted. In this case, the measured capacitance can be described by $C_{min} = \left(\frac{d_{MoS}}{\varepsilon_{MoS}} + C_g^{-1}\right)^{-1}$, where ε_{MoS} and d_{MoS} are the dielectric constant and the thickness of MoS_2, respectively. This allows us to directly obtain the ε_{MoS}–d_{MoS} relationship of MoS_2. To accurately extract $\varepsilon_{MoS} = \frac{d_{MoS}}{C_{min}^{-1} - C_g^{-1}}$, the geometric capacitance C_g should be carefully treated. Here, an interlayer capacitance C_{in} originated from the interlayer spacing between BN and MoS_2 is included in the calculation of $C_g = (C_{BN}^{-1} + C_{in}^{-1})^{-1}$, where C_{BN} is the geometric capacitance of BN. This interlayer capacitance has been applied in previous studies on twisted bilayer graphene[38–40]. Here we estimate this interlayer capacitance $C_{in} \sim 25.3\,\mu F\,cm^{-2}$ with the interlayer dielectric constant $\sim 10\varepsilon_0$ and interlayer spacing ~ 0.35 nm[38,40]. The extracted ε_{MoS} with and without including the interlayer capacitance are both shown in Fig. 2.

As shown in Fig. 2, ε_{MoS} has been found to increase from $\sim 4\varepsilon_0$ for a monolayer to $\sim 11\varepsilon_0$ for bulk MoS_2. This is in excellent agreement with theoretical predictions[41,42]. The small ε_{MoS} in monolayer MoS_2 suggests poor dielectric screening of Coulomb interactions, indicating that strong electron–electron interactions could be achieved in clean monolayer MoS_2. The largely increased mobility observed in monolayer MoS_2 placed in a high-κ dielectric environment[2,3,43] probably benefits from its small ε_{MoS}. In fact, the decrease in the optical phonon mode E_{2g}^1 observed by a Raman spectroscopy study of few-layer and bulk MoS_2 (ref. 44) is also due to the strong dielectric screening effects.

The valence band of multilayer MoS_2 is also accessed by detecting the inversion layer of holes using low excitation frequencies at sufficiently high temperatures (Fig. 3a,b). However, the inversion layer is invisible when using high frequencies at low temperatures ($T < 100$ K). This is due to the presence of the Schottky barrier between the Ti/Au contact and the valence band[7]. Holes must form through thermal excitations or minute current leakage into the contacts. This process often requires a long time from $\sim$ms to seconds. In the 12-nm-thick MoS_2 capacitance device, the majority of hole carriers have been relaxed around 20 kHz at 300 K, as confirmed by the phase information of the device, which is defined by $\Theta = \arctan(G/2\pi f C_t)$, where G is the conductance. As shown in Fig. 3c, the phase peaks appear at ~ 20 kHz for different negative gate bias voltages, indicating that

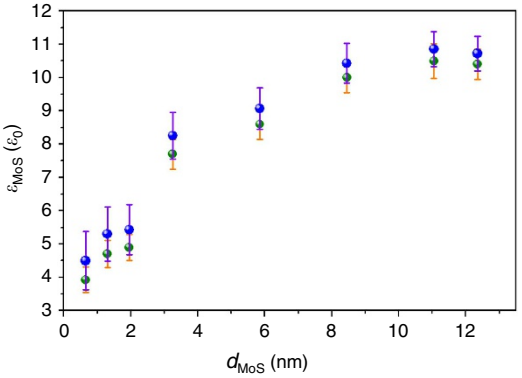

Figure 2 | Experimental data of the thickness-dependent dielectric constant of MoS_2. The dielectric constant of MoS_2 ε_{MoS} with (blue dots) and without (green dots) including interlayer capacitance is plotted as a function of thickness d_{MoS}. ε_{MoS} increases from $\sim 4\varepsilon_0$ for a monolayer to $\sim 11\varepsilon_0$ for bulk MoS_2. The errors originate from the measurements of sample sizes, thicknesses of MoS_2 and BN, and capacitances of MoS_2.

the relaxation time of holes in the 12-nm-thick MoS_2 device is around 50 μs. For the capacitance samples contacted by Cr/Au top electrodes (Cr has a larger work function (~ 4.5 eV) than that of Ti (~ 4.3 eV)), a short relaxation time (~ 5 μs) for holes has also been achieved at 300 K (Supplementary Fig. 5 and Supplementary Note 4).

By applying the Poisson equation to model the vertical heterostructures in a quasi-quantitative manner (Supplementary Note 5), we correlated the quantum capacitance of MoS_2 C_q with the surface potential V_s in our capacitance devices. V_s is extracted based on the charge conservation relation $V_s = \int_0^{V_g} (1 - \frac{C_t}{C_g}) dV_g$. To accurately extract C_q, the interlayer capacitance between BN and MoS_2 C_{in} is included. Owing to the finite thickness of MoS_2 (< 15 nm) and the vertical configuration of the capacitance device, the MoS_2 capacitance in vertical structure $C_{MoS} = (C_t^{-1} - C_g^{-1})^{-1}$ is a non-zero value C_{s0} inside the bandgap (Supplementary Figs 6 and 7). The quantum capacitance of MoS_2 C_q can be described by $C_q = C_{MoS} - C_{s0}$ (Supplementary Fig. 8). The C_q–V_s relation is shown in Fig. 3d, yielding a band gap around 1.14 eV, which is close to the reported value of 1.2 eV[45]. The quantum capacitance of monolayer MoS_2 is shown in Supplementary Fig. 9, which shows a smaller value compared with that in multilayer MoS_2 (Supplementary Note 6). As our measurements are performed near the band edge of MoS_2 and a large amount of disorders are present in MoS_2, the quantum capacitance is not saturated to the predicted value 57.6 $\mu F\,cm^{-2}$ (corresponding to a density of states $\sim 3.6 \times 10^{14}\,eV^{-1}\,cm^{-2}$ (refs 14,46)) beyond the mobility edge. The dashed line above breaks in Fig. 3d schematically shows the expected quantum capacitance at higher Fermi energies.

Percolation-induced MIT in monolayer and multilayer MoS_2. Similar to the MIT observed in transport measurements[3–6], the capacitance data of the 5.9-nm-thick MoS_2 device measured at different temperatures (Fig. 4m) show an interesting transition with a well-defined cross-over point (at $V_g = 5$ V and corresponding to a carrier density $n \sim 6.8 \times 10^{12}\,cm^{-2}$, obtained from $n = C_g(V_g - V_s - V_T)/e$, where $V_T \sim -1$ V is the threshold voltage). When $V_g < 5$ V C_t decreases with decreasing temperature, whereas at $V_g > 5$ V the temperature dependence of C_t is reversed. The observed cross-over point in capacitance measurements is indeed related to the MIT as its value ($\sim 6.8 \times 10^{12}\,cm^{-2}$) is consistent with that measured by

© 2015 Macmillan Publishers Limited. All rights reserved.

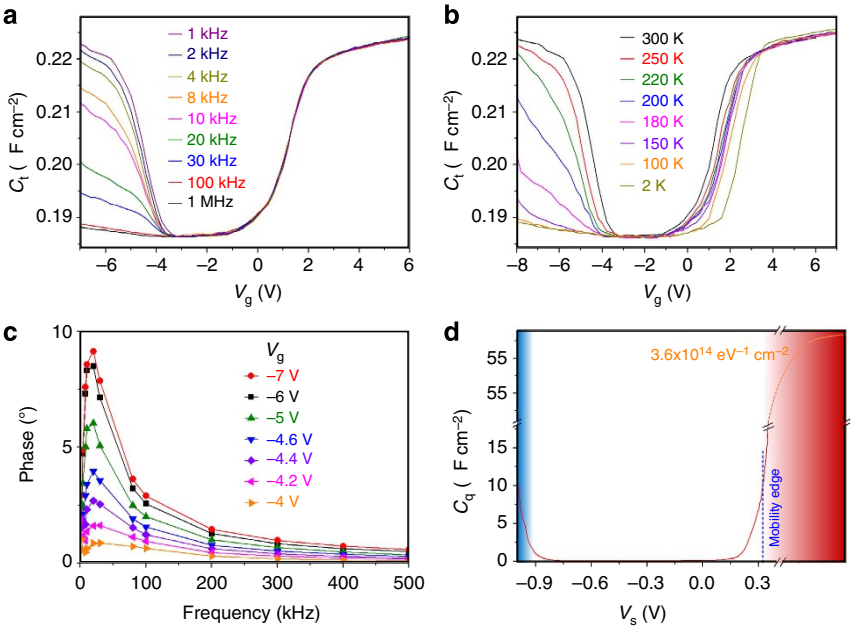

Figure 3 | The valence band of multilayer MoS_2 accessed by capacitance measurement. (**a**) C_t measured at 300 K for different excitation frequencies. (**b**) C_t measured at 1 kHz for different temperatures. (**c**) Phase information plotted as a function of excitation frequencies at 300 K for different V_g. The phase peak around 20 kHz yields a relaxation time of hole carriers at 50 μs. (**d**) The quantum capacitance C_q of MoS_2 plotted as a function of surface potential V_s at 300 K, which yields a band gap width of around 1.14 eV. The excitation voltage used is 100 mV. The dashed line above breaks schematically shows the expected quantum capacitance at higher Fermi energies.

transport (ref. 6 and Fig. 6). More evidence is provided by capacitance measurements of monolayer MoS_2 samples (Fig. 5a). In monolayer MoS_2, the intersections of the capacitance curves showed obvious temperature-dependent characteristics. At temperatures below 100 K, we observed that the cross-over point was stabilized roughly at $n \sim 1.2 \times 10^{13}\,cm^{-2}$, consistent with the transport results measured in monolayer MoS_2 (ref. 3) with an MIT at $n \sim 1 \times 10^{13}\,cm^{-2}$. Bilayer and trilayer MoS_2 samples displayed similar transition phenomena with cross-over points around $n \sim 8.6 \times 10^{12}\,cm^{-2}$ (Fig. 5b).

The electronic transport of MoS_2 suffers from charge impurities[2,3] and short-range disorders[12,14,19,20], such as ripples, dislocation and sulphur vacancies. These disorders result in the insulating transport behaviour of MoS_2 in the low carrier-density region, where electrons transport through hopping between localized states (Fig. 4h) and can be well described by the variable-range-hopping model[3,12,20]. In the region where sufficient, large carrier densities are introduced, metal behaviour is observed[3]. Here we propose a percolation-type MIT in MoS_2, driven by density inhomogeneity of electron states[28–35] that describes the systems in which charge carriers are transported through percolating conductive channels in the disorder landscapes due to the poor screening effect at low carrier densities. When carrier density is low enough, conductive paths are efficiently blocked and MIT occurs. MoS_2 has been proven to be such a disordered system, with impurity concentration ranging from 10^{11} to $10^{13}\,cm^{-2}$, especially for monolayer MoS_2, which is more vulnerable to ripples and charge impurities[2,3,12,14,19,20]. Thus, the MIT in MoS_2 is in line with the percolation transition theory in which disorder plays an important role. Moreover, our capacitance and transport data, shown below, provide further evidences to this effect.

The evolution of concentration and effective thickness of electron states probed by capacitance measurements can explain the observed MIT in transport measurements fairly well and provide details of the percolation transition process. The percolation transition phenomenon is illustrated in Fig. 4h–j. With increasing carrier densities n (by increasing gate voltage), the localized electron states begin to percolate with each other till a conductive channel occurs at a critical density (Fig. 4i). Further increasing carrier densities will lead to sufficient conductive channels spanning the entire system and result in metal-like transport behaviours (Fig. 4j). On the other hand, at the same carrier density, the effective thickness $d_{eff} = \varepsilon_{MoS}/C_{MoS}$ of electron states confined in the surface of MoS_2 can be tuned by varying temperatures (Fig. 4l). Smaller d_{eff} can also be achieved at higher gate voltages where large amounts of surface charges are induced (supported by theoretical calculations in the Supplementary Note 5). As illustrated in Fig. 4e–g (assuming n remains unchanged), more conductive channels are formed at a smaller d_{eff}. The MIT should occur when d_{eff} is sufficiently small. The capacitance data of our samples (Fig. 4l,m) are similar to those obtained from transport measurements in multilayer MoS_2 (showing an MIT at $n = 6.7 \times 10^{12}\,cm^{-2}$) (ref. 6). When $n < 6.8 \times 10^{12}\,cm^{-2}$, d_{eff} decreases with increasing temperatures. Hence, the conductivity should increase as the temperature increases. In contrast, when $n > 6.8 \times 10^{12}\,cm^{-2}$, the increase of d_{eff} would lead to decreasing conductivity as the temperature increases. Furthermore, the increasing n and decreasing d_{eff} would also enhance the screening of disorders and electron states, and thus lead to increasing conductivity, while lowering the Coulomb interaction strength. It is noticed that the effective channel thickness is only applicable to multilayer MoS_2, as monolayer MoS_2 is a truly 2D system. The percolation transition in monolayer MoS_2 mainly results from the tuning of concentration of electron states at different gate voltages. An alternative explanation on the transition is based on the quantum capacitance of MoS_2, which is closely related to the carrier density ($C_q = e^2 \frac{\partial n}{\partial E_F}$) and the effective channel thickness. A larger quantum capacitance suggests a larger density of states or a smaller effective channel thickness. Therefore, the observed

© 2015 Macmillan Publishers Limited. All rights reserved.

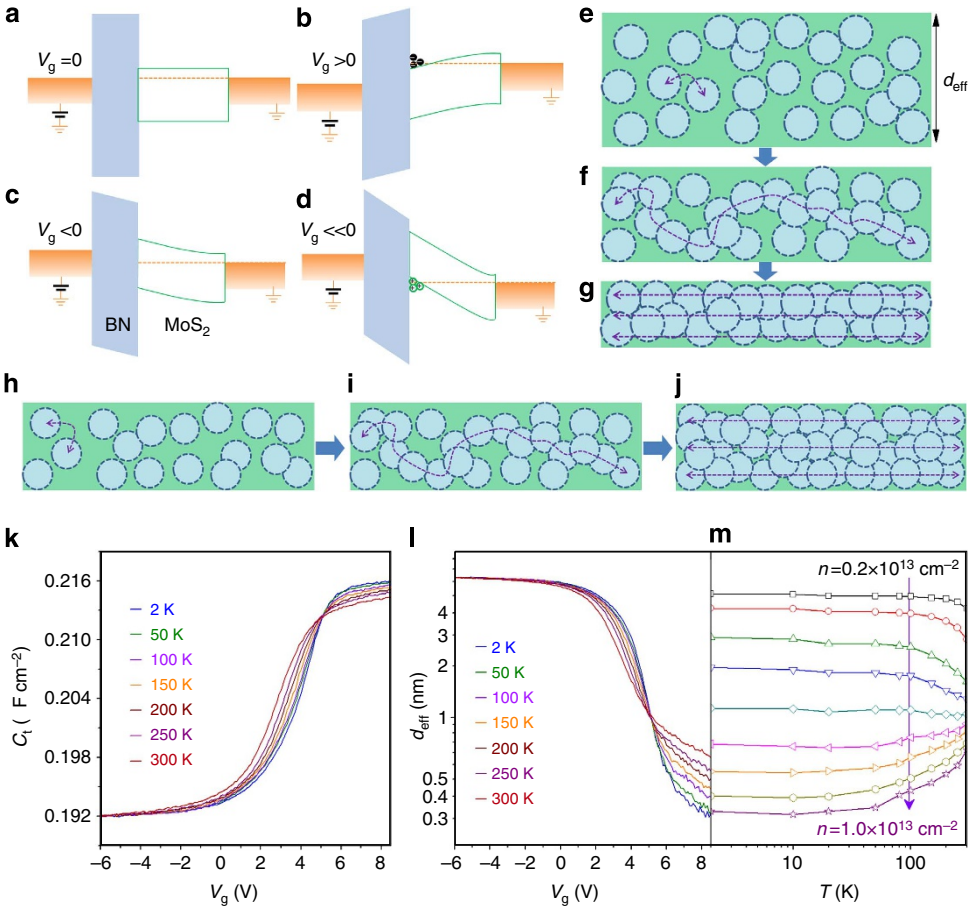

Figure 4 | The percolation transition driven by density inhomogeneity in multilayer MoS_2. (**a**–**d**) The schematic band diagrams of metal-BN-MoS_2-metal structures at flat band (**a**), accumulation region (**b**), depletion region (**c**) and inversion region (**d**). (**e**–**j**) The schematic images showing the percolation-induced MIT under different effective thicknesses of electron states (**e**–**g**) and carrier densities (**h**–**j**). The circles denote isolated carrier puddles in MoS_2. (**k**,**l**) The measured total capacitance C_t (**k**) and effective thickness d_{eff} (**l**) plotted as a function of gate voltage V_g for 2–300 K. The excitation voltage and frequency used are 50 mV and 100 kHz, respectively. (**m**) d_{eff} plotted as a function of temperatures at different carrier densities n.

gate-tuned transition from insulating to metallic region is the direct consequence of the increase of quantum capacitance with increasing gate voltages (as shown in Fig. 3d).

The percolation transition also suggests an increasing transition density at the cross-over point with increasing impurity concentration[30–32]. In our MoS_2 samples, the transition density was in the range 10^{12}–10^{13} cm^{-2} due to the presence of large amounts of impurities. Moreover, the transition density in monolayer MoS_2 ($\sim 1\times10^{13}$ cm^{-2}) was larger than that observed in multilayer MoS_2 ($\sim 6\times10^{12}$ cm^{-2}), which agreed with the prediction of percolation theory as monolayer MoS_2 was more vulnerable to disorders. This was further evidenced by extracting charge trap densities, D_{it}, of MoS_2 from capacitance measurements (a trilayer sample shown in Fig. 5c). The presence of impurities or disorder may cause charge-trapping effects in MoS_2 capacitance devices, particularly at low temperatures. The charge traps can be fully excited only at relatively low frequencies (for example, 100 Hz). The density of the charge traps can then be estimated by measuring the difference in capacitance at low and high frequencies, that is, $D_{it}=(C_{MoS}(low_f)-C_{MoS}(high_f))/e$. The trap densities in our monolayer and trilayer MoS_2 samples were in the order of 10^{12} eV^{-1} cm^{-2} (Fig. 5d). The trap densities in monolayer MoS_2 were apparently large, suggesting that monolayer MoS_2 is more sensitive to disorder. In fact, the trap densities in our samples were underestimated because of the limitation of the excitation frequency ranges. At relatively high temperatures (inset of Fig. 5c), the charge traps were easily excited and the capacitances measured at low and high frequency show no difference.

The percolation-induced MIT in MoS_2 is further supported by transport data at low temperatures. The MITs of multilayer (Fig. 6a) and monolayer (Fig. 6b) MoS_2 are clearly shown by the conductivity σ, at different temperatures, similar to previous reports[3–6]. The MIT occurs at $n\sim 6\times10^{12}$ cm^{-2} for multilayer MoS_2 and $n\sim 1.1\times10^{12}$ cm^{-2} for monolayer MoS_2, consistent with the capacitance data. The mobilities of the monolayer and multilayer MoS_2 samples measured at 2 K are around 90 and 250 cm^2 V^{-1} s^{-1}, respectively (Supplementary Fig. 10 and Supplementary Note 7). To gain further insight into the transition behaviour, we applied the percolation model of conductivity[31,32,35] near the percolation threshold density n_c, which is described by

$$\sigma = A(n-n_c)^{\delta} \quad (1)$$

where A is a constant of proportionality and δ is the percolation exponent. Below the threshold density n_c, the 2D electron gas broke up into isolated puddles of carriers, with no conducting channels crossing the whole sample. The conductivity showed insulating behaviour and eventually vanished at $T=0$ K. In 2D systems, δ is expected to be 4/3 and a cross-over point ($\sim e^2/h$) above the percolation threshold density is suggested at finite temperatures[30,31]. Based on the percolation model, we fit our

© 2015 Macmillan Publishers Limited. All rights reserved.

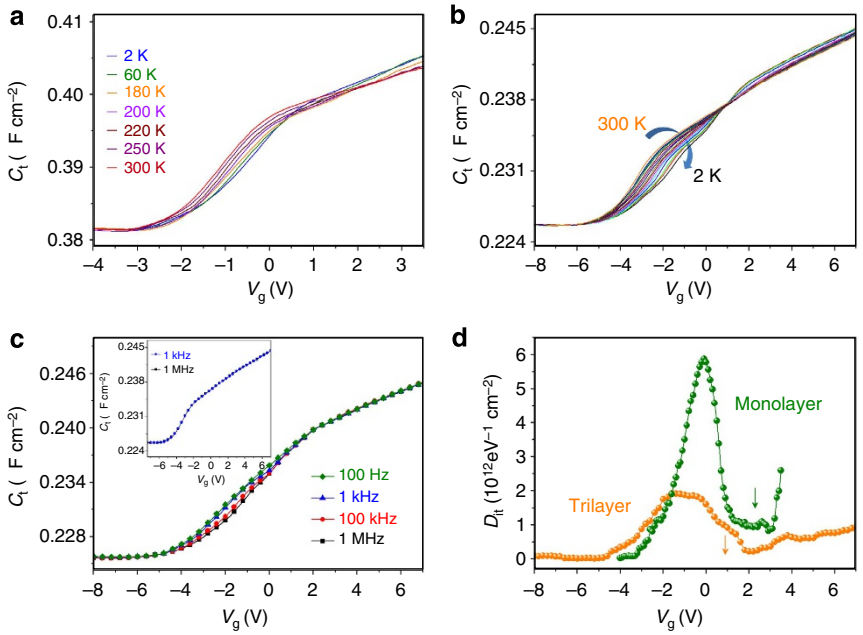

Figure 5 | The percolation transition and charge traps in monolayer and trilayer MoS_2. (**a**) C_t of a monolayer MoS_2 measured at an excitation frequency 1 kHz and excitation voltage 50 mV for different temperatures. (**b**) C_t of a trilayer MoS_2 measured at an excitation frequency 100 kHz. (**c**) C_t of a trilayer MoS_2 measured for different excitation frequencies at 2 K, indicating that the charge traps are excited at low frequencies. The inset shows C_t measured at 300 K. (**d**) The charge-trap densities D_{it} as a function of V_g calculated for the monolayer and trilayer MoS_2 samples. The arrows denote the transition points.

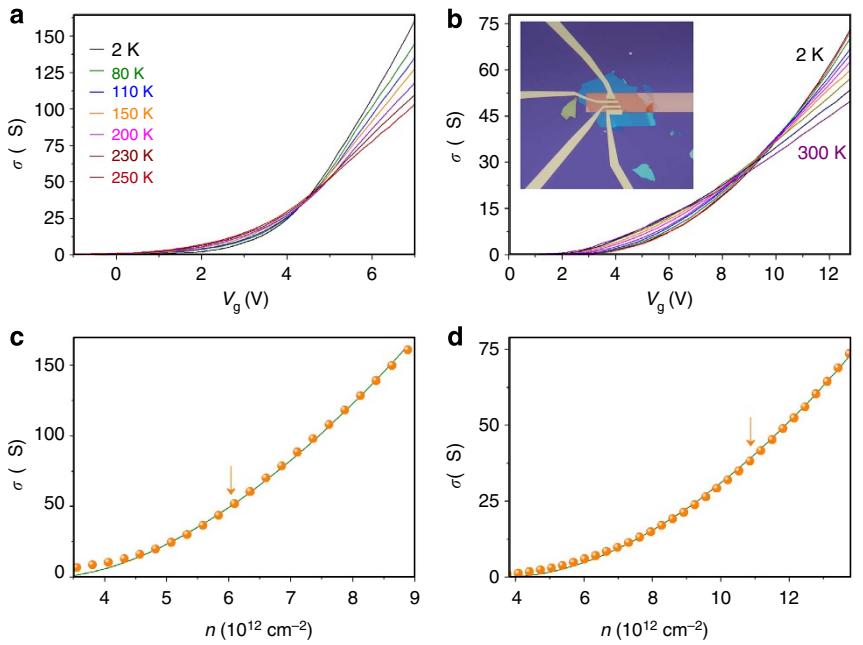

Figure 6 | Transport results showing the percolation transition in multilayer and monolayer MoS_2. (**a**,**b**) The MITs are clearly shown by σ measurements of a multilayer (**a**) and monolayer (**b**) MoS_2 for different temperatures. The inset in **b** shows the optical image of a monolayer MoS_2 device. (**c**,**d**) The fitting of experimental σ (orange dots) of multilayer (**c**) and monolayer (**d**) MoS_2 according to the percolation conductivity $\sigma = A(n - n_c)^{\delta}$ (green lines). The arrows denote the positions of MITs.

experimental data of multilayer (Fig. 6c) and monolayer (Fig. 6d) MoS_2 samples at 2 K. The experimental results show excellent agreement with theoretical predictions near the transition point. The extracted parameters are $\delta \sim 1.7$ and $n_c \sim 3.2 \times 10^{12}\,cm^{-2}$ in multilayer MoS_2 and $\delta \sim 1.8$ and $n_c \sim 3.8 \times 10^{12}\,cm^{-2}$ in monolayer MoS_2. The obtained percolation exponents are consistent with experimental values $\delta = 1.4$–1.7 found in other 2D systems, such as GaAs/AlGaAs heterostructures[31,32]. The obtained percolation threshold density n_c is lower than the value of MIT cross-over point (mobility edge) because of thermal activation of localized electron states. n_c would approach the mobility edge when temperature is sufficiently low. The percolation transition model can be applied only near the transition point at low temperatures. In the metallic region with

© 2015 Macmillan Publishers Limited. All rights reserved.

higher carrier densities, the conductivity would show a linear increase with gate voltages where the conductivity is mainly limited by the linearly screened charge impurity scattering[31]. The slight deviation between experimental data and fitting curves at low carrier densities is due to enhanced hopping conductivity and quantum tunnelling at finite temperatures.

Discussion

One alternative scenario besides the percolation transition model is the phase transition theory for a metallic phase (stabilized by *e*–*e* interactions) and an insulating phase (disorder prevails over *e*–*e* interactions), which are separated by a quantum critical point[3,47]. This theory shows the existence of the quantum critical point where the density of states of the underlying collective modes is divergent at the transition point. The transport data obtained from MoS_2 cannot provide more information for distinguishing these divergent collective modes. In contrast, the capacitance measurement is able to probe the global behaviour of these divergent collective modes, which would lead to a divergent quantum capacitance at the transition point[22,25,47]. In our capacitance experiments, however, the divergent quantum capacitance was not observed around the transition point. The capacitance data seems to be more inclined to the density inhomogeneity induced by disorder, which dominates the properties at the MIT transition point, as the Coulomb interactions of electrons could be suppressed by a large amount of disorder existing in MoS_2. Based on our transport and capacitance data, the percolation transition model is more consistent with the MIT phenomena in MoS_2.

The vertical MIS heterostructures built from atomically thin MoS_2 are ideal capacitor structures for probing the electron states and intrinsic properties of MoS_2. According to the analyses of experimental data obtained by electrical transport measurement and capacitance spectroscopy, we believe that the percolation-type MIT (driven by density inhomogeneities of electron states) is the dominating mechanism of the MIT in both monolayer and multilayer MoS_2. The vertical heterostructures offer the added advantages of eliminating the influence of large impedance at the band tails and accessing intrinsic characteristics such as thickness-dependence dielectric constant and band gap variation in atomically thin MoS_2. The present study also provides a new approach to characterizing the intrinsic properties of other atomically thin-layered materials and interface states of heterostructures built from 2D materials.

Methods

Sample preparation. Monolayer and multilayer MoS_2 flakes were exfoliated from MoS_2 crystals (from 2D semiconductors) by the micromechanical cleavage technique. MoS_2 and BN flakes were placed on the surface of a glass slide coated with Polydimethylsiloxane/Methyl methacrylate as described for graphene-BN device fabrication[36]. Next, these thin flakes were transferred onto a local Ti/Au (10 nm/20 nm) gate. The top electrodes were patterned using standard electron-beam lithography. Two types of top electrodes, Ti/Au (10 nm/50 nm) and Cr/Au (2 nm/50 nm), were fabricated through electron-beam evaporation. The dielectric constant of the BN sheet is measured by calibrating an internal reference capacitor that sits near the MoS_2 capacitance device (Fig. 1a). The thicknesses of MoS_2 and BN flakes were measured by an atomic force microscope (Veeco-Innova).

Capacitance and transport measurements. Capacitance measurements were carried out using an HP Precision 4284A LCR Meter with a sensitivity of $\sim$0.1 fF in a cryogenic system (2–300 K). All wires in the measurement circuits were shielded and the p-Si substrates were also grounded to minimize residual capacitance. The residual capacitance in the measurement setup is at the order of 1 fF (see Supplementary Fig. 3). Transport measurements were performed in the same cryogenic system using lock-in techniques.

References

1. Novoselov, K. S. *et al.* Two-dimensional atomic crystals. *Proc. Natl Acad. Sci. USA* **102,** 10451–10453 (2005).
2. Radisavljevic, B., Radenovic, A., Brivio, J., Giacometti, V. & Kis, A. Single-layer MoS_2 transistors. *Nat. Nanotechnol.* **6,** 147–150 (2011).
3. Radisavljevic, B. & Kis, A. Mobility engineering and a metal-insulator transition in monolayer MoS_2. *Nat. Mater.* **12,** 815–820 (2013).
4. Baugher, B. W. H., Churchill, H. O. H., Yang, Y. F. & Jarillo-Herrero, P. Intrinsic electronic transport properties of high-quality monolayer and bilayer MoS_2. *Nano Lett.* **13,** 4212–4216 (2013).
5. Schmidt, H. *et al.* Transport properties of monolayer MoS_2 grown by chemical vapor deposition. *Nano Lett.* **14,** 1909–1913 (2014).
6. Ye, J. T. *et al.* Superconducting dome in a gate-tuned band insulator. *Science* **338,** 1193–1196 (2012).
7. Kim, S. *et al.* High-mobility and low-power thin-film transistors based on multilayer MoS_2 crystals. *Nat. Commun.* **3,** 1011 (2012).
8. Lee, G. H. *et al.* Flexible and transparent MoS_2 field-effect transistors on hexagonal boron nitride-graphene heterostructures. *ACS Nano* **7,** 7931–7936 (2013).
9. Britnell, L. *et al.* Strong light-matter interactions in heterostructures of atomically thin films. *Science* **340,** 1311–1314 (2013).
10. Lopez-Sanchez, O., Lembke, D., Kayci, M., Radenovic, A. & Kis, A. Ultrasensitive photodetectors based on monolayer MoS_2. *Nat. Nanotechnol.* **8,** 497–501 (2013).
11. Yoon, Y., Ganapathi, K. & Salahuddin, S. How good can monolayer MoS_2 transistors be? *Nano Lett.* **11,** 3768–3773 (2011).
12. Ghatak, S., Pal, A. N. & Ghosh, A. Nature of electronic states in atomically thin MoS_2 field-effect transistors. *ACS Nano* **5,** 7707–7712 (2011).
13. Wang, Q. H., Kalantar-Zadeh, K., Kis, A., Coleman, J. N. & Strano, M. S. Electronics and optoelectronics of two-dimensional transition metal dichalcogenides. *Nat. Nanotechnol.* **7,** 699–712 (2012).
14. Zhu, W. J. *et al.* Electronic transport and device prospects of monolayer molybdenum disulphide grown by chemical vapour deposition. *Nat. Commun.* **5,** 3087 (2014).
15. Liu, K. K. *et al.* Growth of large-area and highly crystalline MoS_2 thin layers on insulating substrates. *Nano Lett.* **12,** 1538–1544 (2012).
16. Zhan, Y. J., Liu, Z., Najmaei, S., Ajayan, P. M. & Lou, J. Large-area vapor-phase growth and characterization of MoS_2 atomic layers on a SiO_2 substrate. *Small* **8,** 966–971 (2012).
17. Mak, K. F., He, K. L., Shan, J. & Heinz, T. F. Control of valley polarization in monolayer MoS_2 by optical helicity. *Nat. Nanotechnol.* **7,** 494–498 (2012).
18. Zeng, H. L., Dai, J. F., Yao, W., Xiao, D. & Cui, X. D. Valley polarization in MoS_2 monolayers by optical pumping. *Nat. Nanotechnol.* **7,** 490–493 (2012).
19. Zhou, W. *et al.* Intrinsic structural defects in monolayer molybdenum disulfide. *Nano Lett.* **13,** 2615–2622 (2013).
20. Qiu, H. *et al.* Hopping transport through defect-induced localized states in molybdenum disulphide. *Nat. Commun.* **4,** 2642 (2013).
21. Chen, X. *et al.* Electron-electron interactions in monolayer graphene quantum capacitors. *Nano Res.* **6,** 619–626 (2013).
22. Yu, G. L. *et al.* Interaction phenomena in graphene seen through quantum capacitance. *Proc. Natl Acad. Sci. USA* **110,** 3282–3286 (2013).
23. Hunt, B. *et al.* Massive dirac fermions and Hofstadter butterfly in a van der Waals heterostructure. *Science* **340,** 1427–1430 (2013).
24. Wang, L. *et al.* Negative quantum capacitance induced by midgap states in single-layer graphene. *Sci. Rep.* **3,** 2041 (2013).
25. Chen, X. L. *et al.* Negative compressibility observed in graphene containing resonant impurities. *Appl. Phys. Lett.* **102,** 203103 (2013).
26. Wang, L. *et al.* Detection of resonant impurities in graphene by quantum capacitance measurement. *Phys. Rev. B* **89,** 075410 (2014).
27. Xia, J., Chen, F., Li, J. & Tao, N. Measurement of the quantum capacitance of graphene. *Nat. Nanotechnol.* **4,** 505–509 (2009).
28. He, S. & Xie, X. C. New liquid phase and metal-insulator transition in Si MOSFETs. *Phys. Rev. Lett.* **80,** 3324–3327 (1998).
29. Zhang, Z. Q. & Sheng, P. Quantum-percolation model of electronic transport in 2-dimensional granular metal-films. *Phys. Rev. B* **44,** 3304–3315 (1991).
30. Meir, Y. Percolation-type description of the metal-insulator transition in two dimensions. *Phys. Rev. Lett.* **83,** 3506–3509 (1999).
31. Das Sarma, S. *et al.* Two-dimensional metal-insulator transition as a percolation transition in a high-mobility electron system. *Phys. Rev. Lett.* **94,** 136401 (2005).
32. Manfra, M. J. *et al.* Transport and percolation in a low-density high-mobility two-dimensional hole system. *Phys. Rev. Lett.* **99,** 236402 (2007).
33. Adam, S., Cho, S., Fuhrer, M. S. & Das Sarma, S. Density inhomogeneity driven percolation metal-insulator transition and dimensional crossover in graphene nanoribbons. *Phys. Rev. Lett.* **101,** 046404 (2008).
34. Shashkin, A. *et al.* Percolation metal-insulator transitions in the two-dimensional electron system of AlGaAs/GaAs heterostructures. *Phys. Rev. Lett.* **73,** 3141–3144 (1994).
35. Das Sarma, S. & Hwang, E. H. Charged impurity-scattering-limited low-temperature resistivity of low-density silicon inversion layers. *Phys. Rev. Lett.* **83,** 164–167 (1999).

© 2015 Macmillan Publishers Limited. All rights reserved.

36. Zomer, P. J., Dash, S. P., Tombros, N. & van Wees, B. J. A transfer technique for high mobility graphene devices on commercially available hexagonal boron nitride. *Appl. Phys. Lett.* **99,** 232104 (2011).
37. Dean, C. R. *et al.* Boron nitride substrates for high-quality graphene electronics. *Nat. Nanotechnol.* **5,** 722–726 (2010).
38. Sanchez-Yamagishi, J. D. *et al.* Quantum hall effect, screening, and layer-polarized insulating states in twisted bilayer graphene. *Phys. Rev. Lett.* **108,** 076601 (2012).
39. Schmidt, H. *et al.* Tunable graphene system with two decoupled monolayers. *Appl. Phys. Lett.* **93,** 172108 (2008).
40. Fallahazad, B. *et al.* Quantum Hall effect in Bernal stacked and twisted bilayer graphene grown on Cu by chemical vapor deposition. *Phys. Rev. B* **85,** 201408 (2012).
41. Cheiwchanchamnangij, T. & Lambrecht, W. R. L. Quasiparticle band structure calculation of monolayer, bilayer, and bulk MoS_2. *Phys. Rev. B* **85,** 205302 (2012).
42. Molina-Sanchez, A. & Wirtz, L. Phonons in single-layer and few-layer MoS_2 and WS_2. *Phys. Rev. B* **84,** 155413 (2011).
43. Min, S. W. *et al.* Nanosheet thickness-modulated MoS_2 dielectric property evidenced by field-effect transistor performance. *Nanoscale* **5,** 548–551 (2013).
44. Lee, C. *et al.* Anomalous lattice vibrations of single- and few-layer MoS_2. *ACS Nano* **4,** 2695–2700 (2010).
45. Kam, K. K. & Parkinson, B. A. Detailed photocurrent spectroscopy of the semiconducting group VIB transition metal dichalcogenides. *J. Phys. Chem.* **86,** 463–467 (1982).
46. Larentis, S. *et al.* Band offset and negative compressibility in graphene-MoS_2 heterostructures. *Nano Lett.* **14,** 2039–2045 (2014).
47. Punnoose, A. & Finkel'stein, A. M. Metal-insulator transition in disordered two-dimensional electron systems. *Science* **310,** 289–291 (2005).

Acknowledgements

We are grateful for fruitful discussions with Professor Z.Q. Zhang from HKUST. Financial support from the Research Grants Council of Hong Kong (Project Numbers HKU9/CRF/13G, 604112, HKUST9/CRF/08, N_HKUST613/12 and HKUST-SRFI) and technical support of the Raith-HKUST Nanotechnology Laboratory for the electron-beam lithography facility at MCPF (Project Number SEG_HKUST08) are hereby acknowledged.

Author contributions

X.C. is the main contributor, who initiated and conducted most experiments including sample fabrication, data collection and analyses. N.W. is the principle investigator and coordinator of this project. X.C., N.W. and P.S. provided the physical interpretation and wrote the manuscript. The remaining authors provided technical assistance in sample preparation, data collection/analyses and experimental setup.

Additional information

Supplementary Information accompanies this paper at http://www.nature.com/naturecommunications

Competing financial interests: The authors declare no competing financial interests.

Reprints and permission information is available online at http://npg.nature.com/reprintsandpermissions/

How to cite this article: Chen, X. *et al.* Probing the electron states and metal-insulator transition mechanisms in molybdenum disulphide vertical heterostructures. *Nat. Commun.* 6:6088 doi: 10.1038/ncomms7088 (2015).

© 2015 Macmillan Publishers Limited. All rights reserved.